Measurement of transient force produced by a propagating arc magnetohydrodynamic plasma actuator in quiescent atmospheric air

Measurement of transient force produced by a propagating arc magnetohydrodynamic plasma actuator in quiescent atmospheric air

Young Joon Choi, Jayant Sirohi and Laxminarayan L Raja

Department of Aerospace Engineering and Engineering Mechanics, The University of Texas at Austin, Austin, TX 78712, USA

E-mail: jayant.sirohi@mail.utexas.edu and lraja@mail.utexas.edu

CrossMark

Abstract

An experimental study was conducted on a magnetohydrodynamic plasma actuator consisting of two parallel, six inch long, copper electrodes flush mounted on an insulating ceramic plate. An electrical arc is generated by a $\sim$1 kA current pulse at $\sim$100 V across the electrodes. A self-induced Lorentz force drives the arc along the electrodes. The motion of the arc induces flow in the surrounding air through compression as well as entrainment, and generates a transient force, about $\sim$4 ms in duration. Experiments were performed on a prototype actuator in quiescent atmospheric air to characterize the motion of the arc and the momentum transferred to the surrounding air. Measurements included transient force and total impulse generated by the actuator as well as the armature voltage and current. The arc shape and transit velocity were determined by high-speed imaging. A peak force of 0.4 N imparting an impulse of 0.68 mN-s was measured for a peak current of 1.2 kA. The force scaled with the square of the armature current and the impulse scaled linearly with the spent capacitor energy. The results provide insight into the mechanisms of body force generation and momentum transfer of a magnetohydrodynamic plasma actuator.

Keywords: force, actuator, magnetohydrodynamic, plasma, deconvolution, impulse, air

(Some figures may appear in colour only in the online journal)

1. Introduction

Plasma actuators can affect the aerodynamic flow over a body by imparting momentum to the surrounding air. Their benefits for flow control include low mass, absence of moving parts, and high control bandwidth [1]. Plasma actuators can be broadly classified as either thermal, electrohydrodynamic (EHD) or magnetohydrodynamic (MHD). Thermal actuators include sparkjets [2] that simply provide rapid heating of the gas which indirectly imparts momentum to the flow through dilatational effects. EHD actuators such as the dielectric barrier discharge (DBD) provide direct momentum transfer to the flow through electric field forcing of non-zero space-charge regions of the plasma, while MHD actuators rely on external or self-induced magnetic fields to realize Lorentz force momentum transfer to the flow.

For low-speed, atmospheric pressure aerodynamic flows, EHD actuation by DBDs has been widely studied for a variety of applications [3]. However, as shown by numerous experimental and supporting modeling studies, their performance is limited by velocity saturation, force saturation, and performance variability resulting from charge deposition on the dielectric surfaces [4–6]. Consequently, experimental demonstrations of DBD actuators have been limited to low Mach number ($<$0.1) and Reynolds number regimes ($<$10^6) at atmosphere [7].

Pulsed Power Supply
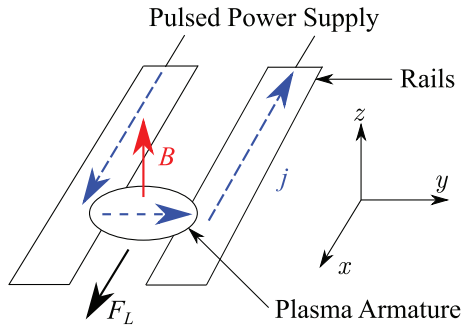
Figure 1. Schematic illustrating RailPAc operation. Current density through the rails (*j*) induces a net magnetic field (***B***) in the *z*-direction between the rails. The current density through the armature in the *y*-direction couples with (***B***) to impart a Lorentz force (***F***L) in the *x*-direction.

Magnetohydrodynamic (MHD) plasma actuators have been proposed for control of high-speed flows, albeit at low pressures (Mach number 5–10, static pressure 1.4–5.5 kPa) [8]. More recently, our group proposed an MHD rail plasma actuator (RailPAc) suitable for atmospheric pressure flow actuation applications [9]. The RailPAc geometry (figure 1) comprises two parallel electrodes (rails) that are flush mounted on an insulating (ceramic) plate. The rails are connected to a pulsed power supply that can generate a high current (~1 kA) at ~100 V for a short duration (~ms). An electrical breakdown of the air gap between the rails creates an arc, or plasma armature. The plasma armature completes a current loop with current density (*j*) that induces a magnetic field (***B***). As a result, the armature experiences a Lorentz force (***F***L) in the direction along the rails. The Lorentz force accelerates the plasma armature along the rails, and the motion of the armature induces flow in the surrounding air through a combination of compression and entrainment effects [9].

Past studies on RailPAc include both experimental characterizations and numerical simulations to assess its potential for flow control applications. Pafford *et al* [9] tested a prototype RailPAc and measured an induced velocity of approximately 10 m s⁻¹ at a Reynolds number of 0.45 million. High-speed video taken by Pafford *et al* [9] revealed a highly complex transit of the plasma armature. Indeed, several previous studies by authors have shown that a transient arc experiencing Lorentz force undergoes significant transformation in arc shape and arc root attachment characteristics depending on the discharge geometry and operation [10–12]. A satisfactory explanation for most important features of the transient moving arc in the RailPAc is possible only if the force and impulse characteristics of the arc are available in addition to the electrical characteristics and visible imaging of arc motion.

The key performance metric of a flow control actuator is its control authority. This can be defined as the momentum transferred by the actuator to the surrounding air, which is equal to the impulse generated by the actuator. Studies on pulsed plasma devices that act on a similar time scale as the RailPAc (~4 ms), such as pulsed DBD actuators [13] and MHD thrusters [14–16], have been limited to quantifying
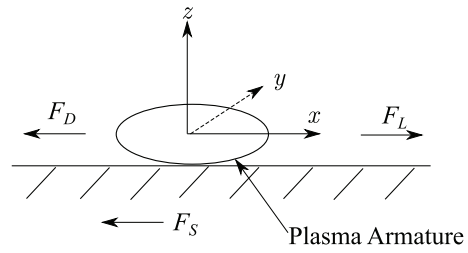
Figure 2. The balance of forces acting on the plasma armature in *x*-direction (direction of transit). The component of Lorentz force in *x*-direction (F_L) accelerates the armature. The armature motion induces flow by compression and entrainment of the surrounding air. The armature experiences aerodynamic drag (F_D) and surface drag (F_S) that reduces armature transit velocity.

total impulse delivered. While impulse measurement gives the actuator control authority, the time history of the force applied to the surrounding air yields insight into the physical mechanisms. However, it is challenging to measure a small transient force due to contamination of the measurement by the structural response of the actuator supports. Several studies [17–19] have shown that the structural modes can be removed from the transient force measurement using deconvolution. This process uses an impulse response function to formulate an inverse problem that reconstructs the force from the structural response. However, the force measurements using deconvolution that have been reported in the literature are limited to large impact forces compared to that expected from the RailPAc.

The objective of this paper is to measure the transient force generated by a RailPAc. This measurement will be verified by an independent measurement of the total impulse. Correlation of the measured transient force with the time resolved electrical measurements as well as the high-speed video of the arc transit will yield insight into the physical mechanisms of the operation of the RailPAc.

2. Physical principles

The Lorentz force accelerates the plasma armature along the rails (figure 2), resulting in compression of the air ahead of the armature and entrainment of air in its wake. The equation of motion of the armature is given by

$$m_a \ddot{x} + \dot{m}_a \dot{x} = F_L - F_D - F_S \qquad (1)$$

where m_a is the armature mass, x is the position of the armature along the rails, F_L is the Lorentz force, F_D is the volumetric aerodynamic drag, and F_S is a force that describes the drag due to proximity of the armature to the RailPAc surface. Note that the first term on the left-hand side is the acceleration term and the second is the 'snowplow' term, which accounts for the increase in mass of the armature as it pushes air along the rails [20]. Equation (1) can be rearranged as

$$F_L - F_S = m_a \ddot{x} + \dot{m}_a \dot{x} + F_D. \qquad (2)$$

The snowplow and the aerodynamic drag terms represent the force acting on the surrounding air. The inertial term describes the momentum gained by the plasma armature,
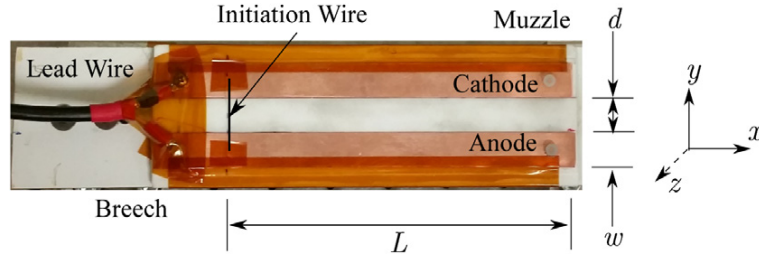
Figure 3. A top view of the RailPAc prototype. The arc propagates along the *x*-direction. The *z*-axis is oriented out of the page. The rails here are separated by a distance $d = 12.75$ mm, have a width $w = 12.7$ mm and are 152 mm long. The distance from initiation to muzzle is $L = 127$ mm.

which is comprised of both ionized air and ablated species from the rails [21]. Thus, the right hand side of equation (2) provides a direct measure of the RailPAc control authority. The total force on the left hand side of equation (2) is the reaction force, F_R, experienced by the RailPAc support structure, i.e. the test stand to which it is mounted. The actuator control authority can be found by integrating the measured transient force in time.

The Lorentz force in equation (2) can be analytically found either from the energy conservation of RailPAc circuit or by solving the MHD equations [22]. The impulse generated by the Lorentz force can be expressed in terms of the power dissipated in the circuit. Let us first define a new coordinate system that is fixed at the center of the armature (figure 2). The *x*-direction of this coordinate system is along the direction of transit and the *y*-direction is along the direction of $\boldsymbol{j}$ in the armature. Recall that the Lorentz force is defined over the armature volume *V* as

$$\boldsymbol{F}_L = \int_V \boldsymbol{j} \times \boldsymbol{B} \quad dV. \tag{3}$$

Evaluation of the integral in equation (3) requires a full description of $\boldsymbol{B}$ field around the RailPAc rails, however, a number of simplifying assumptions can be made. First, the rails are treated as an ideal conductors of infinite length, spaced a distance *d* apart. Second, the armature has a finite length δ along the *x*-direction and a height h_a in the *z*-direction above the RailPAc surface. Third, a uniform current density of magnitude *j* acts solely along the *y*-direction. Finally, a magnetic field of magnitude B_z exists in the *z*- direction between the rails. With these assumptions, equation (3) simplifies to

$$F_L = h_a j d \int_{-\delta/2}^{\delta/2} B_z \quad dx. \tag{4}$$

The magnetic field is given by Ampere's law

$$\nabla \times \boldsymbol{B} = \mu_0 \boldsymbol{j}. \tag{5}$$

The boundary condition for equation (5) can be found by noting that the rails conduct current from the pulsed power supply upto the armature. We therefore assume no current exists in the rails in the *x*-direction for $x > \delta/2$, which leads to zero induced magnetic field for $x > \delta/2$, neglecting end effects. Thus, a suitable boundary condition for equation (5) is

$$B_z(\delta/2) = 0. \tag{6}$$

With the boundary condition and equation (5), it can be shown that B_z within the armature decreases linearly from $x = -\delta/2$ to $x = \delta/2$. By using the definition of current density and the solution to equation (5), the Lorentz force can be expressed as

$$F_L = \frac{1}{2} \frac{\mu_0 d}{h_a} i^2 = \frac{1}{2} L' i^2 \tag{7}$$

where μ_0 is the permeability of free space, *i* is the armature current, and L' is the inductance gradient, which is assumed to remain constant.

The impulse generated by the Lorentz force can be obtained by integrating equation (7) over the transit time of the armature (T_t)

$$J_L = \int_0^{T_t} \frac{1}{2} L' i^2 dt. \tag{8}$$

Here, we note that the electrical power dissipated by the RailPAc armature and circuit is given by

$$\Delta E = R \int_0^{T_t} i^2 dt. \tag{9}$$

Assuming constant inductance gradient and combined circuit and plasma resistances (R), the impulse generated by the Lorentz force is directly proportional to the electrical power dissipated.

$$J_L = \frac{1}{2} L' \frac{\Delta E}{R}. \tag{10}$$

3. Experimental methods

A prototype RailPAc (figure 3) was constructed by flush mounting a pair of rails to an insulating ceramic plate. The two parallel copper rails measure 152 mm long, 12.7 mm wide (*w*), and 0.56 mm thick. The rails are spaced 12.7 mm apart (*d*). To initiate the arc, a 0.127 mm diameter aluminum fuse wire is stretched across the gap between the rails and taped to the rail surfaces at a location 25 mm away from one end of the rails. The location of the initiation wire and the rail length limits the maximum transit distance (*L*) to 127 mm. The fuse wire is used to initiate the plasma armature consistently at the same location. The lead wires cross over at a location near the attachment point to the rails. The lead wire attachment side of
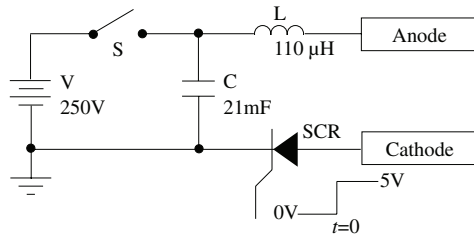
Figure 4. An electrical schematic of the pulse forming network. The switch (S) is opened after the capacitor bank (C) is charged. At trigger time ($t = 0$), a 5V signal is applied to the SCR, a large current discharges through the fuse wire and a plasma armature is formed between the rails.

the rails is referred to as the breech and the opposite end as the muzzle.

The prototype is connected to a pulse forming network (figure 4) consisting of a capacitor bank, series inductor, and trigger circuit. The capacitor bank, comprised of six electrolytic capacitors (Sprague Powerlytic 36DX), is charged to various initial voltages (up to 250V) with a Xantrex XHR 600 dc power supply. The initial capacitor voltage controlled the total energy discharged to the RailPAc. The silicon controlled rectifier (SCR) blocks current flow when its gate voltage is pulled to the ground. Once the capacitors are charged, the SCR gate voltage is pulled up to 5V to initiate the plasma armature. The SCR shorts one rail to the ground and a large current from the capacitor conducts through the fuse wire. This current vaporizes the fuse wire into an ionized conductive channel, and the plasma armature is formed.

The circuit in figure 4 can be modeled as a series RLC circuit with total resistance R equal to the sum of component resistances ($\sim$0.1 Ω) and the armature resistance ($\sim$0.05 Ω). The circuit inductance increases by a small value ($<$0.1% of fixed inductance) due to the transit of the armature along the rails. The natural frequency of the prototype circuit was calculated without considering the changes in the rail inductance and was found to be 105 Hz, corresponding to a half cycle duration of approximately 5 ms.

Experiments were performed to capture high-speed video of the armature transit, and to measure the rail voltage, rail current, transient force and total impulse generated by the RailPAc.

3.1. High-speed imaging

Two high-speed cameras were used to observe the armature shape. A Phantom V5 camera was mounted above the RailPAc prototype to determine armature root positions, velocity, and acceleration. A Phantom Miro M-310 camera was mounted on the muzzle side, to capture the frontal view of the armature and determine the armature height (h_a). High *f*-stop lenses (*f*/22) and small exposure times (1 μs) were used to reduce image saturation from the plasma intensity. The armature root positions were determined by locating the region of highest intensity along the anode and cathode rail edges.

3.2. Electrical measurements

The electrical measurements were conducted with a voltage probe and a Rogowski coil. The National Instruments cDAQ-9172 data acquisition system with NI-9215 BNC expansion boards sampled the electrical signals at 60kHz. A Rogowski coil, secured between the cathode and the SCR, measured the time rate of change of armature current. This signal was numerically integrated to obtain the current versus time waveform. The voltage across the capacitor was measured using a 1/1000 signal attenuator probe. The energy change in the capacitor and the peak current during the RailPAc was computed based on the electrical measurements. These results were compared to the force and impulse measurements to assess the scaling laws.

3.3. Force measurements

The transient force of the prototype RailPAc was measured on a test stand approximating a single degree of freedom (SDOF) structure. For an accurate measurement without contamination by the structural response, the natural frequency of the test stand must be much higher than the bandwidth of the impulsive forcing. However, the increased stiffness required for the high natural frequency would result in poor force sensitivity. Therefore, in a practical test setup, the measurement will consist of the transient force as well as the structural response of the test stand. In our experiments, the time history of the unknown force is deconvoluted from the known test stand response [17]. Recall that the response of a SDOF structure to an arbitrary forcing $f(t)$ is given by the convolution integral

$$y(t) = \int_0^t g(t - \tau)f(\tau)\mathrm{d}\tau = g(t) * f(t). \quad (11)$$

The response $y(t)$ can be the displacement of the test stand, or, when multiplied by a constant calibration factor, the force measured by loadcells on which the structure is mounted. In equation (11), $g(t)$ is the unit impulse response of the structure given by

$$g(t) = \frac{1}{m_{\mathrm{eq}}\omega_d}\mathrm{e}^{-\zeta\omega_n t}\sin(\omega_d t) \quad (12)$$

where m_{eq} is the equivalent mass of the structure (in this case, the test stand), ω_d and ω_n are damped and undamped natural frequencies, and ζ is the damping ratio. The unit impulse response function, is found experimentally by applying a known impulse using an instrumented impulse hammer, and measuring the test stand response. Inoue *et al* [17] proposed that a good estimate of the unit impulse response function can be obtained by Fourier deconvolution if an exponential window function is applied to the measured response. The exponential window is defined as

$$w_e(t) = \mathrm{e}^{-\gamma t}. \quad (13)$$

The optimal γ for a signal without noise is $2\pi/T$ [23], where T is the total duration of the response measurement. For noisy signals, a smaller γ gives better results [17]; for this
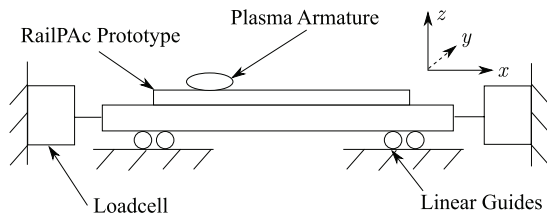
Figure 5. Force test stand designed to measure transient force in *x*-direction. The RailPAc prototype is mounted on linear guides and the test stand displacement is measured using two load cells.

paper, $\gamma = 0.4\pi/T$ was chosen. The test stand response can be derived with a known force and unit impulse response function by discretizing the integral in equation (11) to obtain a system of linear equations

$$y(n) = \sum_{k=0}^{N} \alpha_k f(k) g(n-k) \qquad (14)$$

where α_k are the weights of a chosen quadrature method and *n* is the index of discrete samples. If the sampling interval is small, Riemann quadrature can be used to simplify the expression with $\alpha_k = 1$ for all *k*. The linear equations describing the convolution operator can then be written in matrix form as

$$\boldsymbol{y} = \boldsymbol{Gf}. \qquad (15)$$

The inverse problem to solve for the transient force from the measured response and the unit impulse response function is given by

$$\boldsymbol{f} = \boldsymbol{G}^{-1}\boldsymbol{y}. \qquad (16)$$

Ideally, equation (16) is sufficient to reconstruct the applied force from the measured test stand response. However, any noise in the measured response will result in large oscillations in the deconvoluted force [19]. The effect of noise on deconvolution can be minimized by using regularization, which imposes additional constraints on the inverse problem. Hansen [18] used Tikhonov regularization to stabilize deconvolution by minimizing the residual ε given by

$$\varepsilon = |\boldsymbol{Gf} - \boldsymbol{y}|^2 + \lambda^2 |\boldsymbol{f}|^2. \qquad (17)$$

The constant λ in equation (17) is called a Tikhonov filter factor. Tikhonov regularization solves the deconvolution problem in a least squares sense with $\lambda = 0$ giving the least squares formulation. A suitable choice of λ can smooth out the effect of noise without distorting the desired signal. The process used to determine an optimal λ value and validate the deconvolution procedure can be found in the appendix A.

The RailPAc prototype was placed on the force measurement stand (figure 5), consisting of an Aluminum honeycomb plate mounted on a pair of linear guides, attached to a load cell (Omegadyne LCMFD-20N) on each end. These load cells can measure ±20 N with nonlinearity less than 3 mN. The linear guides constrain the motion of the test stand to the direction of the armature transit, such that the test stand acts as a SDOF structure. Two load cells were used to increase the stiffness of the test stand so that it has a natural frequency at ~300
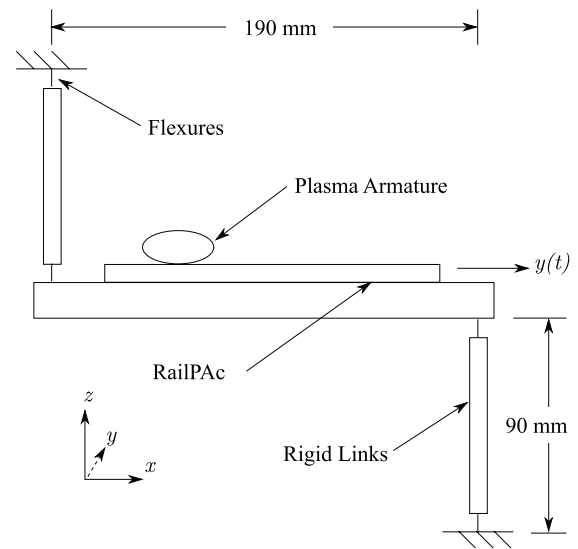
Figure 6. (a) Schematic and (b) picture of the impulse test stand. The pendulums are coupled via a rigid link. The RailPAc prototype is mounted on the link and the displacement of the test stand, *y(t)*, due to RailPAc force is measured using a capacitive displacement sensor.

Hz. The loadcell signals measured from this test stand were deconvoluted to obtain the transient force.

3.4. Impulse measurements

The total impulse generated by the RailPAc was measured in a seperate experiment to verify the measured transient force. The test stand to measure total impulse must have a very low natural frequency so that its oscillation time period is much longer than the duration of the applied transient force. In this case, the transient force can be treated as an ideal impulse. For a lightly damped structure, the applied impulse *J* and maximum displacement of the test stand are linearly proportional

$$J = m_{eq}\omega_d \max(y). \qquad (18)$$

The constants, m_{eq} and ω_d, in equation (18) can be found from the test stand mass and the period of damped oscillation. The RailPAc was mounted on a low natural frequency folded pendulum test stand and the total impulse was obtained by measurement of the test stand deflection. Figure 6 shows a schematic of the test setup. The rigid links act as pendulums, and the hinges are comprised of copper flexures that also serve as electrical connections to the rails. The two pendulums are connected by an aluminum honeycomb panel with the RailPAc prototype mounted on its surface. A low inductance gradient coaxial cable connects the rails to the copper flexures. The pendulums constrain the motion of the test stand along the direction of the armature transit. The displacement of the test stand is measured with a capacitive displacement sensor (capaNCDT 6110 CS05) with a measurement range of 0.5 mm and 75 nm resolution. The test stand has a damped natural frequency of 0.73 Hz and ζ of 0.012.
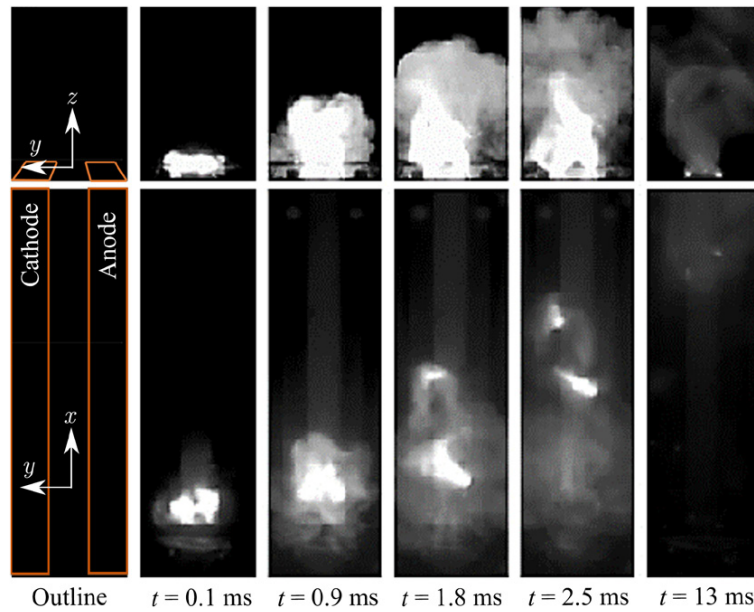
Figure 7. Images of the plasma armature transit. Selected views for $t = 0.1$ ms, 0.9 ms, 1.8 ms, 2.5 ms, and 13 ms referenced from the discharge initiation are shown. The muzzle view provides the vertical dimension of the armature, while the top view shows the location of the armature along the rail. The rectangles indicate the outlines of the rails.

The equivalent mass of the test stand m_{eq} is given by [24]

$$m_{eq} = \frac{I_u}{L_u^2} + \frac{I_l}{L_l^2} + m. \tag{19}$$

The moments of inertia of the upper and lower pendulums, I_u and I_l, were computed by approximating the components as rectangular cuboids with 9.00 ± 0.01 cm in length (L_u and L_l) and 0.70 ± 0.01 cm in thickness rotating about their ends. The uncertainty associated with the length is the sum of the uncertainty in pivot location of the flexures and measurement error. The uncertainty associated with the combined RailPAc prototype and rigid link mass (m) is 0.1 g based on the measurement error. The resulting equivalent mass of the test stand was 610 ± 3 g. The m_{eq} and ω_d values gives impulse test stand calibration factor of 2.8 ± 0.2 mN-s mm^{-1}. The impulse test stand calibration was verified by applying a known impulse (using the instrumented impulse hammer) and measuring the resulting test stand displacement.

4. Results

4.1. High-speed imaging

High-speed video was used to characterize the motion of the plasma armature. As shown in figure 7, the armature undergoes various stages of transit. At the initial stage of transit ($t = 0.1$ ms), the armature can be described as a single filament arc. As the current through the armature increases, the armature increases in intensity ($t = 0.9$ ms) and begins to transit along the rails. The muzzle view shows the armature height during this stage of transit. The armature continues to transit and reduces in luminosity and height due to reduction in the

armature current. At $t = 13$ ms, the armature extinguishes. The images show that a region of diffuse plasma vapor surrounds the armature. This vapor is distinguishable from the armature by the change in intensity between the armature region and the vapor. It has been shown by Parker [25] and Ray [21] that the plasma vapor does not conduct current across the rails. Thus, the armature height, h_a, was determined from the muzzle view by neglecting the vapor region and only considering the height of the armature. This height is shown in figure 8. While the vapor extends to a maximum height of 6 cm from the rail surfaces at $t = 2.5$ ms, the armature height on average was ~2 cm. The armature height was calculated based on the intensity cutoff at 95% of maximum intensity value. The average height was found from the initial 4 ms of transit, during which most of the armature motion occurred. The height estimate demonstrate that the plasma armature interacts with a large volume of the surrounding neutral air.

As shown in figure 8, the transit characteristics of cathode and anode roots are different. While the cathode root transits smoothly along the rails, the anode root moves by sporadic jumps. The anode root attaches to the rail surface until it jumps to a new position closer to the cathode root. This difference in cathode and anode root motion has been documented by several authors [10–12, 26] who also observed the anchoring behavior of the anode root.

The difference in the root motion is explained by the processes required to extract electrons and ions to sustain the arc. In the cathode region, the extraction of electrons is driven by Schottky emission [11], which imposes both local electric field (4×10^7 Vm^{-1}) [27] and electrode surface temperature requirements for the existence of cathode root in a new location. The field enhanced thermionic emission decreases the work function required (4.7 eV to 4.4 eV) to sustain the
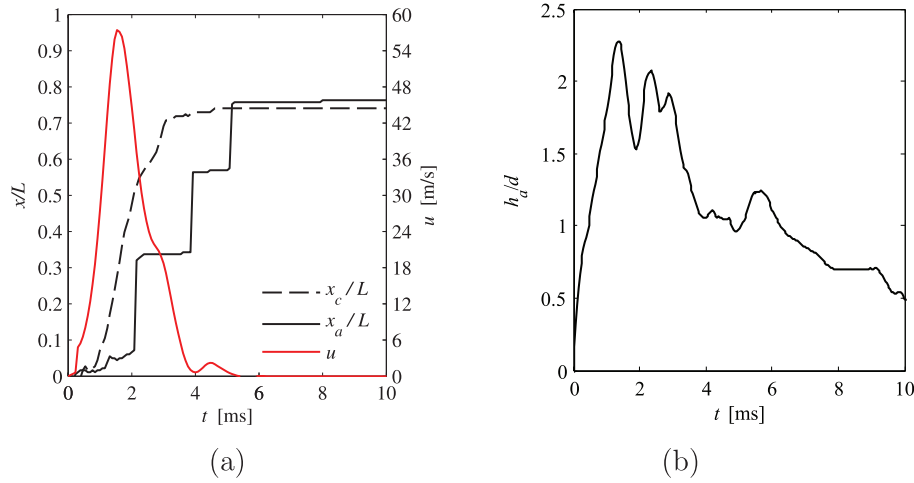
Figure 8. (a) Position of the armature root on the cathode side (x_c) and anode side (x_a). The transit velocity (u) is found by numerical differentiation of x_c. (b) Armature height (h_a) normalized by rail gap (d). Height was determined by outlining the arc shape with 95% of the peak armature intensity.
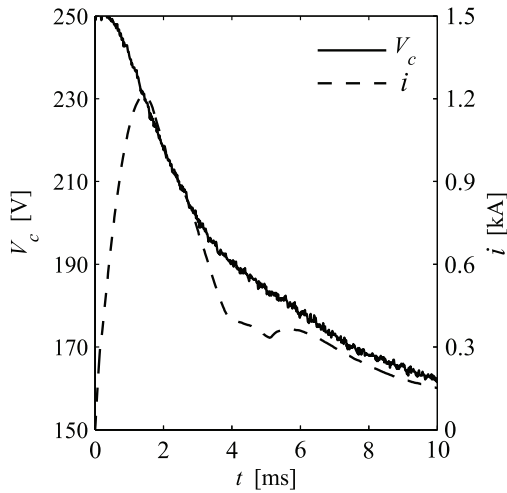
Figure 9. Measured armature current (i) and capacitor voltage (V_c).

armature current, allowing the cathode root to easily transit from one location to another.

On the other hand, the extraction of ions from the anode region requires evaporation of heavier species. Study by Lindmayer showed that the motion of anode root is influenced by the heavy ion evaporation [26]. The temperature requirement for heavy ion evaporation is higher than the extraction of electron. Indeed, the RailPAc anode showed marked evaporation of rail material at the anode root locations. It is evident from the rail topology that the electrode surface temperature required for the vaporization is localized at the anode root and is not present elsewhere on the anode surface. Thus, the anode root is anchored to a particular location to achieve the required temperature condition and its motion requires a secondary breakdown to occur at a new location on the anode.

The secondary breakdown is initiated by the increase in relative distance between the anode and cathode roots. Because the armature resistance scales linearly with the armature

length, the voltage drop between cathode and anode increases due to the lengthening of the armature [28–30]. At certain critical voltage, the anode root forms at a new location near the cathode root to minimize the armature resistance. Since the anode movement requires a breakdown of gap close to the cathode location, the motion appears as disparate jumps.

If the armature current path is approximated as a straight line between the armature roots, it can be shown that the current path is not aligned with the y-axis after $t = 1$ ms. In other words, the current path is not perpendicular to the rails and is rotated by an angle θ from the y-axis. Based on the rail spacing d and armature root locations (x_c and x_a), θ can be approximated as,

$$\theta = \arctan\left(\frac{x_c - x_a}{d}\right). \tag{20}$$

Due to the jumps in the anode root transit, the cathode root position was differentiated numerically to obtain the transit velocity, u. A peak velocity of 56 m s^{-1} was obtained with the armature dissipating at $x/L = 0.75$.

4.2. Electrical measurements

The electrical measurements (figure 9) show a peak current of 1.2 kA for an initial capacitor voltage of 250 V. A large current pulse (~kA) occurs before 5 ms, corresponding to the duration of the armature transit and the half period of the RailPAc circuit. Comparison of the transit velocity and armature height in figure 8 and the armature current in figure 9 reveals a similarity in the velocity and armature height with respect to the current waveform. The discontinuities in di/dt shown in figure 9 correspond to the anode root jumps observed in figure 8. While the anode jumps allow the plasma armature to exist for a longer duration, the armature exhibits little to no motion along the rails after the half period cycle of the RailPAc circuit. The capacitor discharged from $V_c = 250$ V to 100 V, such that only a portion of the capacitor energy was used for the RailPAc operation.

J. Phys. D: Appl. Phys. **48** (2015) 425204

Y J Choi *et al*
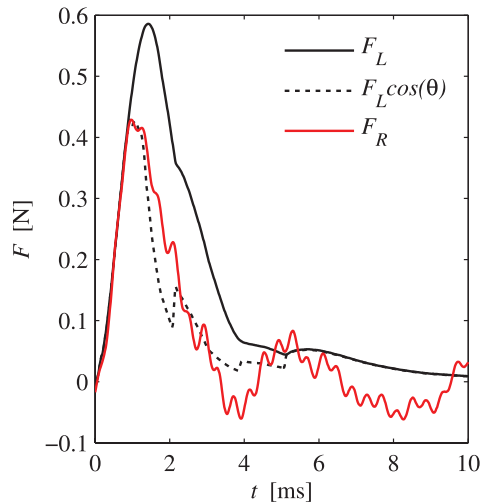
Figure 10. Comparison of the theoretical Lorentz force (F_L), corrected theoretical Lorentz force based on armature orientation ($F_L \cos\theta$), and the reconstructed RailPAc force (F_R).

Figure 11. Maximum measured reaction force ($F_{R,\max}$). A quadratic fit ($F_{R,\mathrm{fit}}$) is provided to determine the scaling of the body force with respect to the armature current ($i_{\max}$).

The capacitor energy expenditure, ΔE, was 560 J, or 85% of the initial capacitor energy, E_0.

4.3. Force measurements

The measured transient force generated by the RailPAc was compared to the theoretical Lorentz force (figure 10) calculated using equation (7), where L' was calculated using the average armature height (2 cm). While the assumption of constant armature height is not reflective of the physcial phenomenon, this simplifying assuption was used by Hariswaran *et al* [31] to sucessfully simulate the RailPac transit. Note that the armature transit excites a higher frequency (transverse bending of honeycomb platform) mode at 2.5 kHz. This was filtered out from the test stand response using a third order polynomial Savitzky–Golay filter with 101 bin size, before reconstructing the transient force.

The theoretical Lorentz force in figure 10 matches the transient force until $t \sim 1$ ms, after which the theoretical force overpredicts the measured force. The discrepancy begins when the arc roots no longer transit together (figure 8). Recall that when the cathode root transits ahead of the anode root, the component of current density along the y-direction scales by $\cos\theta$. If the magnetic field between the rails is assumed to be uniform along the z-direction, then the Lorentz force, as defined in equation (7), must also scale by $\cos\theta$. The corrected theoretical prediction, $F_L \cos\theta$, accounting for the armature orientation closely matches the measured force. Note that there are several assumptions inherent in the theoretical model that are not satisfied in the experimental setup. First, the study by Mercier *et al* [12] showed that the current path between the electrodes is not always linear. Second, the plasma armature after the initial acceleration may not be in local thermal equilibrium. These two effects directly contradict the uniform current density and armature shape assumptions needed to derive equation (7) and may account for some
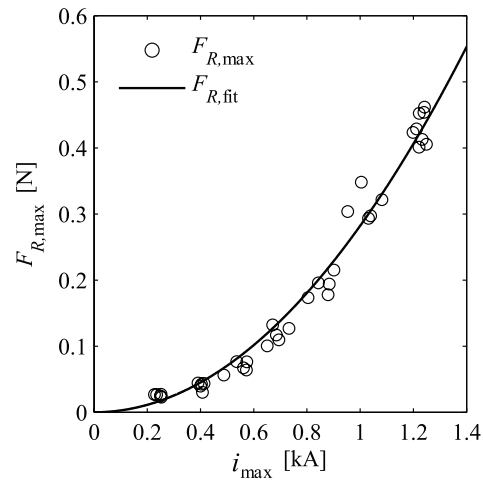
of the discrepancies between the theoretical prediction and measurement.

The theoretical and measured forces suggest that most of the momentum transfer occurred before $t = 4$ ms. The velocity and transit characteristics in figure 8 corroborate this observation since all of the armature motion also occurred before this time. On the other hand, the electrical measurements (figure 9) show that the capacitor bank continues to discharge energy to sustain the armature well after 4 ms. While the energy expenditure up to this point results in a large momentum transfer to the surrounding quiescent air, the subsequent energy expenditure results in little or no momentum transfer. Therefore, the energy expenditure of RaiPAc can be reduced by stopping its operation at $\sim$4 ms without a substantial penalty to the actuator control authority.

4.4. Scaling laws

The RailPAc scaling laws were examined by comparing the force measurements to the electrical measurements. The force scaling law was found by relating the peak force with peak current. As predicted by equation (7), the measured peak force (figure 11) scales quadratically with respect to the peak current.

The impulse scaling law was determined by two methods. First, the impulse delivered to the surrounding air, J^*, was obtained by integrating the measured transient force with respect to time. Second, a direct impulse measurement (J) was performed with the impulse test stand. The results (figure 12) obtained via two methodologies show good agreement. The measurements affirm that RailPAc impulse is linearly proportional to the capacitor energy expenditure. However, the measured impulse (J and J^*) was substantially smaller than the theoretical impulse (J_L). This is ascribed to the inadequacy of the model (equation (10)) since it does not take into account the difference between the cathode and anode transit behavior. The discrepancy between the measured and
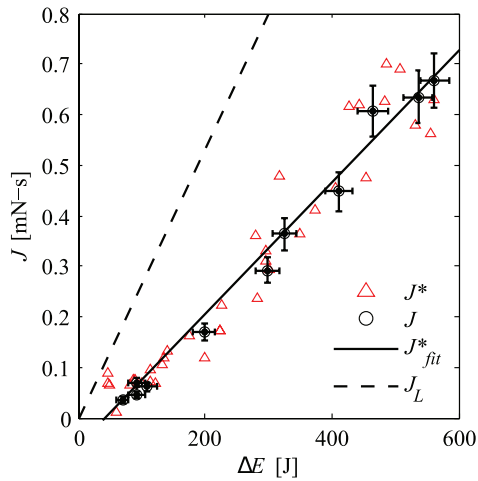
Figure 12. Comparison between the impulse obtained by transient force measurement (J^*) and direct impulse measurement (J). A linear regression of J^* is shown to determine scaling of impulse with respect to the capacitor energy expenditure (ΔE). The theoretical impulse (J_L) is provided for comparison.
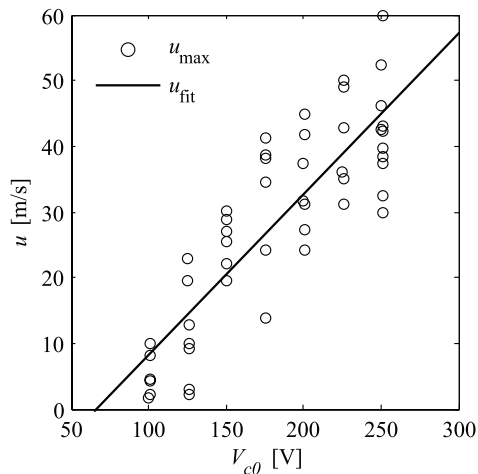
Figure 13. The maximum cathode root transit velocity (u_{max}) as a function of initial capacitor voltage (V_{c0}). A linear regression (u_{fit}) is shown. Large scatter is attributed to the randomness associated with root transit over a used rail surface.

theoretical impulse also suggest that the actuator authority can be improved by minimizing the anode jumps.

Unlike the relationship between energy and impulse found in equation (10), the measured impulse (figure 12) shows a random scatter and an intercept at $\Delta E \sim 50$ J. This energy corresponded to the energy discharged during the intiation stage (<0.5 ms), which was calculated from the voltage and current measurements. Thus, the shift is an initiation energy required to vaporize the fuse wire and form the plasma armature. The scatter in the data about the linear regression line, J_{fit}^*, is ascribed to the changes in the rail surface topology due to rail ablation.

It was observed that the jumps in the anode root motion causes the armature transit velocity (figure 13) as well as the

RailPAc control authority to vary randomly from one firing to another. This variation is caused by surface irregularities on the anode surface. It was suggested by Lindmayer [26] that the condition required to form an armature root is not present on the melted area of the electrode, and the armature root skips over the damaged areas in favor of a new electrode surface. Because the anode root creates a surface degradation about 2 mm in diameter on the rail surface, the locations at which the anode root attaches to the electrode varies with each experiment. The paper reported results from 50 firings, over which no systematic reduction in the control authority or transit velocity could be observed. This is due to the fact that a relatively small portion of the rail is damaged at each transit and the rail still maintains surfaces on which the new anode root can be formed. However, larger number of firings may result in degradation of RailPAc performance. The damage that the electrode sustains can be minimized by decreasing the residence time of the anode root on the surface. A number of studies on gliding arc have focused on this problem and varied electrode geometry [29], material [26], and discharge characteristics. Further studies on implementing the lessons learned in gliding arc should be performed as smooth anode transit may be a crucial enabling technology for the RailPAc.

5. Summary and conclusions

In summary, deconvolution and direct impulse measurements were used to characterize the body force exerted on the quiescent air by a RailPAc. These measurements were made on a prototype RailPAc mounted on force and impulse measurement stands. Test stand responses to the RailPAc body force were measured using loadcells and displacement sensors. Deconvolution in conjunction with Tikhonov regularization was necessary to reconstruct the transient forcing from the measured test stand response and to eliminate the effect of noise. The total impulse was obtained from measurements of the impulse test stand displacement; these measurements agreed well with the reconstructed transient force integrated with respect to time. The RailPAc was determined to impart a peak force of 0.4 N and an impulse of 0.68 mN-s at the initial capacitor voltage of 250 V.

The scaling laws were obtained by comparing force and impulse measurements to electrical measurements. The body force applied to the quiescent air was found to scale quadratically with the peak current while the impulse was found to scale linearly with the total energy disipated by the system. These scaling laws show that the RailPAc can be tailored to a specific flow condition by changing its electrical parameters.

The measured force and impulse can be compared to other plasma actuators. Grossman *et al* reported peak impulse measurement of 2 μN-s with 0.0654 J on a sparkjet [32], while Elias *et al* measured 0.2 mN-s of impulse with 2.7 J of energy on a pulsed DBD of comparable dimension (length of $3d$) [13]. For a DBD operating in steady state actuation, Corke *et al* presented thrust measurement of 0.01 N [33].

J. Phys. D: Appl. Phys. **48** (2015) 425204

Y J Choi *et al*
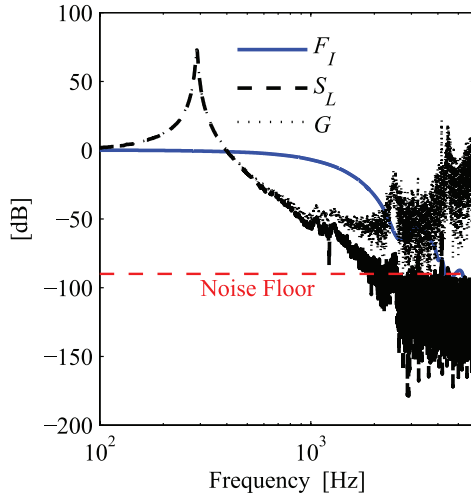
Figure A1. Comparison of power spectrum of the applied forcing (F_I), measured structural response (S_L), and impulse response function ($G(f)$) obtained via deconvolution. For $f \gtrsim 2$ kHz, S_L is dominated by noise and $G(f)$ no longer contains useful information about the structure.

Figure A2. Comparison of the reconstructed forcing F_I^* to the applied forcing F_I for different values of λ.

High speed video was used to study the effect of arc structure on RailPAc control authority. The video revealed that the anode root propagates in sporadic jumps along the rails, leading to a reduction in the measured force and impulse compared to a smooth transit case and random fluctuations in the transit velocity and impulse measurements. Further experimental studies are warranted to characterize the coupling between the measured impulse and the flow field conditions of the surrounding quiescent air.

Appendix A. Validation of the deconvolution procedure

The validation procedure began by characterizing the test stand with an impulse respones function. Tektronix PCB-4461 impulse hammer was used to obtain the unit impulse response function. It has a sensitivity of 2.25 ± 0.53 mV N^{-1} with a resonant frequency at 22 kHz. A steel impact tip was mounted on the impulse hammer to excite the test stand with a short duration (impact duration, $T_h \sim 1$ ms) force, F_I. The output of the load cells is the resulting structural response, S_L. Note that S_L is $y(t)$ in equation (11) scaled by a constant calibration factor.

Figure A1 shows the power spectrum of the applied force, test stand response and the unit impulse response function obtained by deconvolution of the test stand response and the applied force. Note that the applied force is bandwidth limited to f_c of ~ 2 kHz, above which the hammer no longer has sufficient energy to elicit a test stand response. As a result, the loadcell signal decays to the noise floor for $f \gtrsim f_c$. The unit impulse response function no longer contains useful information about the test stand response for $f \gtrsim f_c$, which limits the maximum resolvable forcing bandwidth to around 2 kHz. In other words, deconvolution can only reconstruct a forcing of duration greater than 0.5 ms.
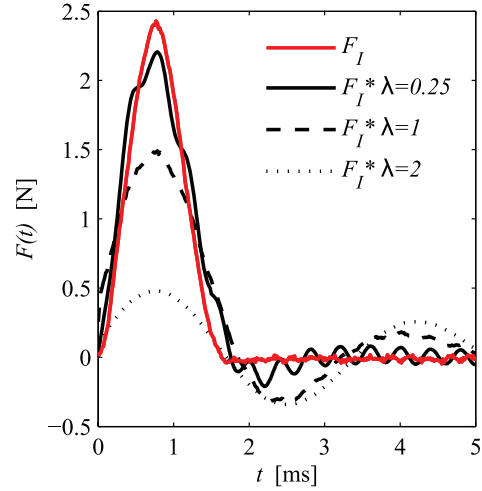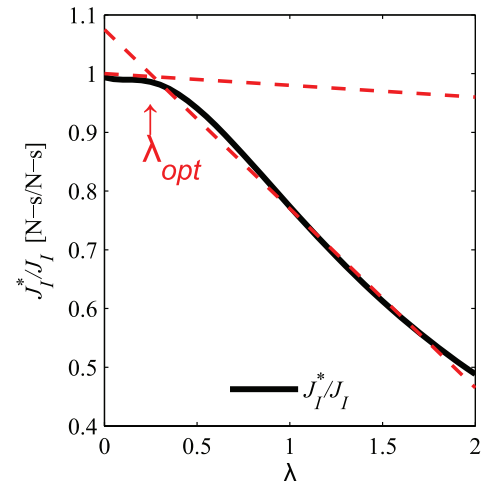
Figure A3. Ratio of the impulse of the reconstructed force (J_I^*) and the impulse of the applied force (J_I). The optimal regularization parameter, λ_{opt}, is found from the transition point at $\lambda = 0.25$.

The deconvolution methodology using Tikhonov regularization was verified by using the impulse hammer with a soft tip to apply an impulse of duration ~ 1.5 ms (representative of RailPAc forcing), and comparing the reconstructed force with the actual applied force. The effect of different values of λ on the reconstructed force F_I^* can be seen in figure A2, where the applied force F_I is measured by the impulse hammer. High values of λ reduce high-frequency oscillations in the reconstructed force, but also decrease the total impulse. Figure A3 shows the effect of λ on the ratio of the reconstructed impulse J_I^*, i.e. the time integral of the reconstructed force (F_I^*), to the applied impulse J_I, i.e. the time integral of the applied force measured by the impulse hammer (F_I). The optimum value of $\lambda_{\mathrm{opt}} = 0.25$ is chosen based on the change of slope of this curve. In general, deconvolution captures the shape of the applied force except at the instants of large $\mathrm{d}F_I/\mathrm{d}t$. This is

a limitation of regularization since the smoothing condition limits the bandwidth of the force that can be reconstructed.

References

[1] Cattafesta L and Sheplak M 2011 Actuators for active flow control *Annu. Rev. Fluid Mech.* **43** 247

[2] Caruana D 2010 Plasmas for aerodynamic control *Plasma Phys. Control. Fusion* **52** 124045

[3] Corke T C, Enloe C L and Wilkinson S P 2010 Dielectric barrier discharge plasma actuators for flow control *Annu. Rev. Fluid Mech.* **42** 505

[4] Likhanskii A V, Shneider M N, Macheret S O and Miles R B 2007 Modeling of dielectric barrier discharge plasma actuators driven by repetitive nanosecond pulses *Phys. Plasmas* **14** 073501

[5] Likhanskii A V, Shneider M N, Opaits D F, Miles R B and Macheret S O 2010 Limitations of the DBD effects on the external flow *48th AIAA Aerospace Sciences Meeting Including the New Horizons Forum and Aerospace Exposition* (*Orlando, FL*) p 470

[6] Boeuf J P, Lagmich Y, Unfer T, Callegari T and Pitchford L C 2007 Electrohydrodynamic force in dielectric barrier discharge plasma actuators *J. Phys. D: Appl. Phys.* **40** 652

[7] Post M L and Corke T C 2004 Separation control on high angle of attack airfoil using plasma actuators *AIAA J.* **42** 2177

[8] Macheret S O, Shneider M N and Miles R B 2004 Analysis of magnetohydrodynamic control of scramjet inlets *AIAA J.* **42** 2303

[9] Pafford B, Sirohi J and Raja L L 2013 Propagating-arc magnetohydrodynamic plasma actuator for directional high-authority flow control in atmospheric air *J. Phys. D: Appl. Phys.* **46** 485208

[10] Velleaud G, Laurent A and Mercier M 1988 A study of the kinematics of a low-voltage breaking self-blown arc: analysis of the derivative of the anode–cathode voltage *J. Phys. D: Appl. Phys.* **22** 933

[11] Teste P, Leblanc T and Chabrerie J-P 1995 Study of the arc root displacement and three-dimensional modelling of the thermal phenomena occuring in a hollow cathode submitted to an electric moving arc *J. Phys. D: Appl. Phys.* **28** 888

[12] Mercier M, Cajal D, Laurent A, Velleaud G and Gary F 1996 Evolution of a low-voltage electric arc *J. Phys. D: Appl. Phys.* **29** 95

[13] Elias P Q and Castera P 2013 Measurement of the impulse produced by a pulsed surface discharge actuator in air *J. Phys. D: Appl. Phys.* **46** 365204

[14] Sasoh A and Yoshihiro A 1993 A high-resolution thrust stand for ground tests of low-thrust space propulsion devices *Rev. Sci. Instrum.* **64** 719

[15] Wilson M J, Bushman S S and Burton R L 1997 A compact thrust stand for pulsed plasma thrusters *25th IEEE Int. Electric Propulsion Conf. (Cleveland, OH)* vol 97 p 765

[16] Burton R L and Turchi P J 1998 Pulsed plasma thruster *J. Propul. Power* **14** 716

[17] Inoue H, Harrigan J J and Reid S R 2001 Review of inverse analysis for indirect measurement of impact force *Appl. Mech. Rev.* **54** 503

[18] Hansen C 2002 Deconvolution and regularization with Toeplitz matrices *Numer. Algorithms* **29** 323

[19] Jacquelin E, Bennani A and Hamelin P 2003 Force reconstruction: analysis and regularization of a deconvolution problem *J. Sound Vib.* **265** 81

[20] Zaidi S H, Smith T, Macheret S and Miles R B 2006 Snowplow surface discharge in magnetic field for high speed boundary layer control *44th AIAA Aerospace Science Meeting and Exhibit (Reno, NV)* p 1006

[21] Ray P K 1989 Arc restrike in the rail accelerator *IEEE Trans. Magn.* **25** 485

[22] Victor K 1997 A study of the equations of motion for plasma-armature railgun *J. Phys. D: Appl. Phys.* **30** 1625

[23] Wilcox D J 1978 Numerical Laplace transformation and inversion *Int. J. Electr. Eng. Educ.* **15** 247

[24] Liu J, Ju L and Blair D B 1997 Vibration isolation performance of an ultra-low frequency folded pendulum resonator *Phys. Lett.* **228** 243

[25] Parker J V 1989 Why plasma armature railguns don't work (and what can be done about it)* *IEEE Trans. Magn.* **25** 418

[26] Lindmayer M 1973 The influence of contact materials and chamber wall materials on the migration and the splitting of the arc in extinction chambers *IEEE Trans. Parts Hybrids Packag.* **9** 45

[27] Yokomizu Y, Matsumura T, Henmi R and Kito Y 1996 Total voltage drops in electrode fall regions of SF_6, argon and air arcs in current range from 10 to 20000 A *J. Phys. D: Appl. Phys.* **29** 1260

[28] Fridman A, Nester S, Lawrence A K, Saveliev A and Mutaf-Yardimci O 1999 Gliding arc gas discharge *Prog. Energy Combust. Science* **25** 211

[29] Kolev S 2015 A 2D model for a gliding arc discharge *Plasma Sources Sci. Technol.* **24** 015025

[30] Nemchinsky V 2014 Arc discharge anode reattachment: simple model *IEEE Trans. Plasma Sci.* **42** 4026

[31] Sitaraman H and Raja L L 2013 Magneto-hydrodynamics simulation study of high speed flow control using the rail plasma actuator (RailPAc) *44th AIAA Plasmadynamics and Lasers Conf. (San Diego, CA)* p 2758

[32] Grossman K R, Cybyk B Z, Rigling M C and Van Wie D M 2004 Characterization of sparkjet actuators for flow control *42nd AIAA Aerospace Sciences Meeting and Exhibit (Reno, NV)* vol 4 p 89

[33] Thomas F O, Corke T C, Iqbal M, Kozlov A and Schatzman D 2009 Optimization of dielectric barrier discharge plasma actuators for active aerodynamic flow control *AIAA J.* **47** 2169